Thermal properties of paramagnetic radiation-induced defects in lithium orthosilicate containing breeder material

Andris Antuzevics[a,b], Arturs Zarins[b,c,*], Anna Ansone[b], Janis Cipa[a], Gunta Kizane[b], Julia M. Leys[d], Regina Knitter[d]

[a] *Laboratory of Spectroscopy, Institute of Solid State Physics, University of Latvia, 8 Kengaraga Street, Riga LV-1063, Latvia*
[b] *Laboratory of Radiation Chemistry of Solids, Institute of Chemical Physics, University of Latvia, 1 Jelgavas Street, Riga LV-1004, Latvia*
[c] *Department of Environmental Science and Chemistry, Faculty of Natural Sciences and Mathematics, Daugavpils University, 1a Parades Street, Daugavpils LV-5401, Latvia*
[d] *Institute for Applied Materials, Karlsruhe Institute of Technology, Karlsruhe 76021, Germany*

Keywords:
Lithium orthosilicate
Ceramic breeder
Radiation-induced defects
Electron paramagnetic resonance
Thermally stimulated luminescence
Spectra simulation
Glow curve and spectra deconvolution

A B S T R A C T

Lithium orthosilicate (Li_4SiO_4) containing ceramics are currently being developed as potential solid-state candidate materials for tritium breeding in future thermonuclear fusion reactors. Under the expected operational conditions, the tritium breeding material will be exposed to the simultaneous influence of several strong energetic factors, for example, radiation, temperature, magnetic field, etc. In the present work, thermal properties of the formed and accumulated paramagnetic radiation-induced defects (containing unpaired electrons) in the Li_4SiO_4 pebbles with a 2.5 wt.% surplus of silicon dioxide (SiO_2) were investigated after irradiation with photons of different types and energies: X-rays with an energy up to 45 keV, gamma rays with an average energy of 1.25 MeV, and *bremsstrahlung* with an energy up to 6 MeV. The photon-irradiated pebbles were analysed using two complementary spectroscopic methods: electron paramagnetic resonance (EPR) and thermally stimulated luminescence (TSL). Individual signals contributing to the acquired EPR spectra, TSL glow curves and spectra were distinguished, deconvoluted and simulated in order to obtain a more detailed understanding about the local structure, electron configuration, and thermal stability of the accumulated radiation-induced defects. The simulation and deconvolution data were also compared with the results, which have been acquired for the long-term neutron-irradiated pebbles from the HICU experiment (High neutron fluence Irradiation of pebble staCks for fUsion).

1. Introduction

Presently, lithium orthosilicate (Li_4SiO_4) containing ceramics with various secondary phases, crystalline structures, grain sizes, microstructures, and pebble diameters are being developed as potential solid-state candidate materials for tritium breeding in future thermonuclear fusion reactors [1–7]. Along with the main task to produce and release tritium, the ceramic breeder pebbles must also be able to withstand the harsh operational conditions of a thermonuclear fusion reactor, for example, an intense neutron and ionising radiation flux, elevated temperatures, a high magnetic field, etc. [8]. The interaction mechanism of radiation with matter depends on the mass, electric charge, and energy of the incident particles [9,10]. The high-energy neutrons produced by the deuterium-tritium thermonuclear fusion reactions interact with atomic nuclei and create knock-on atomic displacements, collision cascades, or nuclear transmutation reactions. The kinetic energy of the generated tritium and helium particles by the nuclear transmutation reactions of lithium during irradiation with neutrons is lost when the positively charged energetic particles decelerate in the crystalline lattice of the ceramic breeder pebbles by inelastic interactions (leading to direct ionisation and excitation) and elastic collisions (leading to atomic displacements and collision cascades). The high-energy photons (electromagnetic radiation) created by various nuclear transmutation reactions, deceleration of charged particles, or radioactive decay of the formed unstable atomic nuclei interact with matter in three main ways (indirect ionisation): (1) photoelectron emission; (2) Compton scattering, or (3) positron-electron pair formation. The secondary electrons created by the direct and indirect ionisation of atoms and molecules also have enough energy to produce direct ionisation, excitation, and single atomic displacements. The formed and accumulated electron and hole type radiation-induced point defects (simple centres), their aggregates (complex centres), and radiolysis products can interact with the generated tritium and helium par-

* Corresponding author at: Laboratory of Radiation Chemistry of Solids, Institute of Chemical Physics, University of Latvia, 1 Jelgavas Street, Riga LV-1004, Latvia.
E-mail address: arturs.zarins@lu.lv (A. Zarins).

ticles [11–13], thereby considerably influencing their further diffusion processes and retention in the crystal grains of the ceramic breeder pebbles [14,15].

The HICU experiment (High neutron fluence Irradiation of pebble staCks for fUsion) was performed from February 2008 to December 2010 at the High Flux Reactor (HFR) in Petten, Netherlands [8,16]. The aim of the experiment was to test and evaluate the thermomechanical behaviour of different ceramic breeder materials, including Li_4SiO_4 pebbles with a 2.5 wt.% surplus of silicon dioxide (SiO_2), under conditions that are relevant to the operational parameters of the tritium breeding material in a thermonuclear fusion reactor. The post-irradiation examination (PIE) of the long-term neutron-irradiated Li_4SiO_4 pebbles from the HICU experiment was performed by Kolb et al. [17], Heuser et al. [18], and Leys et al. [19]. The obtained results revealed the formation and accumulation of several paramagnetic radiation-induced defects and radiolysis products (containing unpaired electrons) that are characteristic for irradiated lithium silicates [20]: E' centres (≡Si•), non-bridging oxygen hole centres, also abbreviated as HC_1 and HC_2 (≡Si-O•), peroxide radicals (≡Si-O-O•) or other oxygen-related hole centres, small and large colloidal lithium (Li_n) particles, etc. The symbol "≡" represents three covalent bonds of a silicon atom to three oxygen atoms in the crystalline structure and "•" represents an unpaired electron. A heterogeneous colour change (darkening) was reported, which can be attributed to the formation of colour centres: optically active radiation-induced point defects, their aggregates, or radiolysis products [21]. A significant increase of the secondary phase lithium metasilicate (Li_2SiO_3) was also detected, which originates from the nuclear transmutation reactions of lithium with neutrons, also called as lithium burn-up. In addition, the formation of cracks, open and closed pores, material fractures, and accumulation of the Li_2SiO_3 phase at the grain boundaries were observed.

The main aim of the present work is to obtain a more detailed understanding about the individual structure, electronic configuration, and thermal stability of the formed and accumulated paramagnetic radiation-induced defects in the Li_4SiO_4 pebbles with a surplus of SiO_2 using a more diverse methodology for electron paramagnetic resonance (EPR) and thermally stimulated luminescence (TSL) measurements. Up to now, information in the literature about parameters obtained from the EPR spectra simulations and TSL glow curve and spectra deconvolutions for the formed and accumulated radiation-induced defects in the neutron-irradiated Li_4SiO_4 pebbles is limited. Therefore, the novelty of this work is to combine data acquisition at different settings with stepwise annealing experiments of the irradiated Li_4SiO_4 pebbles and perform numerical modelling to extract the individual signals contributing to the acquired EPR spectra, TSL glow curves and spectra. Simulation parameters are indispensable for reliable identification and local structure assignment of radiation-induced defects. The Li_4SiO_4 pebbles were irradiated with photons of different types and energies instead of neutrons to introduce radiation-induced defects and to separately simulate photon-induced primary and secondary effects, while avoiding nuclear transmutation reactions and consequently the formation of radioactive atomic nuclei. The simulation and deconvolution data of EPR and TSL are also compared with the results, which have been acquired for neutron-irradiated Li_4SiO_4 pebbles with a natural abundance ratio of lithium isotopes from the HICU experiment [19].

2. Experimental

2.1. Analysed samples

The Li_4SiO_4 pebbles with a 2.5 wt.% surplus of SiO_2 (pebble size distribution: 250–630 μm) were fabricated using a melt-spraying process at Schott AG (Mainz, Germany) [22]. In order to achieve the relevant operational crystalline phase composition and homogenous granular microstructure and to remove physically absorbed and chemisorbed water (H_2O) vapour and carbon dioxide (CO_2), the fabricated pebbles were thermally pre-treated at 900 °C for 3 weeks in air using a muffle furnace. The crystalline phase composition was confirmed using powder X-ray diffractometry (p-XRD, Bruker D8) and attenuated total reflection-Fourier transform infrared (ATR-FTIR) spectroscopy methods (Bruker Vertex 70v). Due to the surplus of SiO_2, the thermally pre-treated pebbles consist of two main crystalline phases: monoclinic Li_4SiO_4 as the primary phase and orthorhombic Li_2SiO_3 as the secondary phase. The content of main constituents and trace elements (impurities) was determined using X-ray fluorescence (XRF, Pioneer S4 – Bruker AXS) and inductively coupled plasma optical emission spectrometry methods (ICP-OES, iCAP 7600 – ThermoFisher-Scientific). The detected noble metal impurities, for example, platinum (0.0059 ± 0.0001 wt.%), result from the fabrication process, due to the surface corrosion of the platinum alloy crucible during the melting process of the raw materials, whereas all other metal impurities, for example, aluminium (0.0029 ± 0.0003 wt.%), calcium (0.0021 ± 0.0001 wt.%), sodium (0.0008 ± 0.0001 wt.%), and potassium (0.0006 ± 0.0001 wt.%), can be traced back to the raw materials [23].

2.2. Sample irradiation and isochronal annealing

The thermally pre-treated pebbles were irradiated with X-rays with an energy up to 45 keV, by gamma rays with an average energy of 1.25 MeV, and by *bremsstrahlung* with an energy up to 6 MeV. The irradiation experiments with X-rays were carried out using a custom-built setup equipped with an X-ray tube (tungsten anode, anode voltage: 45 kV, anode current: 10 mA, irradiation time: 30 min, ambient temperature, air). The absorbed dose of the X-ray irradiated pebbles is evaluated to be about 1 kGy. The irradiation experiments with gamma rays were carried out using a cobalt-60 isotope source (absorbed dose: 10 kGy, dose rate: 2.28 kGy h^{-1}, ambient temperature, air). The irradiation experiments with *bremsstrahlung* were carried out using a linear electron accelerator and a target material consisting of copper with additions of tungsten (absorbed dose: 1 kGy, dose rate: 14 Gy min^{-1}, ambient temperature, air). The low absorbed doses were selected in order to induce mainly the formation of primary radiation-induced point defects, while excluding the accumulation of radiation-induced defect aggregates and radiolysis products.

The photon-irradiated pebbles were isochronally annealed in a custom-built furnace in air with an estimated temperature uncertainty of ± 5 °C. The pebbles were inserted at the selected temperature, kept for 10 min, and rapidly cooled to ambient temperature by removing the sample from the furnace.

2.3. Characterisation methods

The formed and accumulated paramagnetic radiation-induced defects in the photon-irradiated pebbles before and after isochronal annealing were investigated using EPR spectroscopy. The EPR measurements were performed employing a Bruker Elexsys-II E500 spectrometer with three different settings:

(1) X-band (9.83 GHz), ambient temperature.
(2) X-band (9.37 GHz), low temperature (10–100 K).
(3) Q-band (33.89 GHz), ambient temperature.

The distinction between sample annealing temperature and EPR spectra acquisition temperature needs to be highlighted, which is emphasised by a selection of different units. The annealing temperature denotes the heating temperature of the sample, and it is

indicated in degrees Celsius. The acquisition temperature refers to sample temperature in Kelvin during EPR spectra detection.

EPR spectra acquisition parameters were: 0.2–200 mW microwave power, 0.1 mT magnetic field modulation amplitude, and 100 kHz modulation frequency. Unless specified otherwise, the EPR measurements were conducted at ambient temperature in air. EPR spectra simulations of individual signals were performed in EasySpin software [24]. EasySpin's function *esfit* was used for the least-squares fitting procedure of the experimental spectra.

Radiative recombination processes of the formed and accumulated radiation-induced defects (resulting in luminescence) in the photon-irradiated pebbles before and after isochronal annealing were investigated using the TSL technique. For the TSL glow curve and spectra measurements, the irradiated pebbles were carefully powdered at ambient temperature in air using an agate mortar in order to exclude the influence of heterogenous distribution of radiation-induced defects in the pebble volume [25].

TSL glow curves were measured from ambient temperature up to 400 °C with a heating rate of 2 °C s^{-1} in air using custom-built equipment consisting of a temperature controller coupled with a heating element and an Agilent 34907A multichannel digital voltmeter connected to a photomultiplier tube. TSL glow curves were deconvoluted in GlowFit software. Herein, non-linear functions describing single glow peaks were fitted to experimental points using the least-squares Levenberg-Marquardt method [26].

TSL spectra were measured in a 280–850 nm range using stainless steel cups with 10 mm diameter from ambient temperature up to 500 °C with a heating rate of 1 °C s^{-1} in a nitrogen atmosphere. The measurements were performed using a Lexsyg Research TL/OSL reader (Freiberg Instruments Ltd.), which was connected to an Andor Sr-303i-B spectrometer equipped with a DV420A-BU2 camera (150 l/mm, blaze 500 nm) by an ultra-low -OH Molex optical fibre. To reduce the influence of thermal radiation, Schott short bandpass filter KG3 was used. TSL spectra were deconvoluted in Origin software using energy-based Gaussian functions [27].

3. Results and discussion

3.1. Electron paramagnetic resonance (EPR)

EPR spectra of the Li_4SiO_4 pebbles after irradiation with neutrons and photons of different types and energies are shown in Fig. 1. No EPR signals were detected prior to the irradiation. EPR spectra of the irradiated pebbles are almost identical in shape and centred at 351 mT ($g = 2.00$), which is consistent with the results reported for lithium silicate materials exposed to X-rays, gamma rays, accelerated electrons, and neutrons [14,19,21,28–32]. It is expected that the form, size, and structure (spurs, blobs, short and branch electron tracks) of the interaction site of photons depend on their energy, interaction mechanism, and the energy of the created secondary electrons. Nevertheless, the observed minor differences in the EPR spectra are probably due to the different absorbed doses. The formation and accumulation of radiation-induced defects in ceramic materials usually take place through two main primary stages [33]. In the first stage (fast process), mobile charge carriers (electrons and holes) created by the indirect and direct ionisation are trapped both, on intrinsic defects (crystalline lattice imperfections) and extrinsic defects (impurity atoms). As described previously, the content of metal impurities in the analysed pebbles is negligible (<0.01 wt.%). Therefore, the trapping of the created electrons and holes on extrinsic defects can be ruled out. The first stage dominates until all intrinsic defects are gradually consumed during irradiation. In the second stage (slow process), electronic excitation mechanism (radiolysis) and single knock-on atomic displacements proceed depending on the energy of photons and secondary electrons, thereby slightly reducing the crystallinity, and further generating intrinsic defects in the crystalline lattice of the primary and secondary phases.

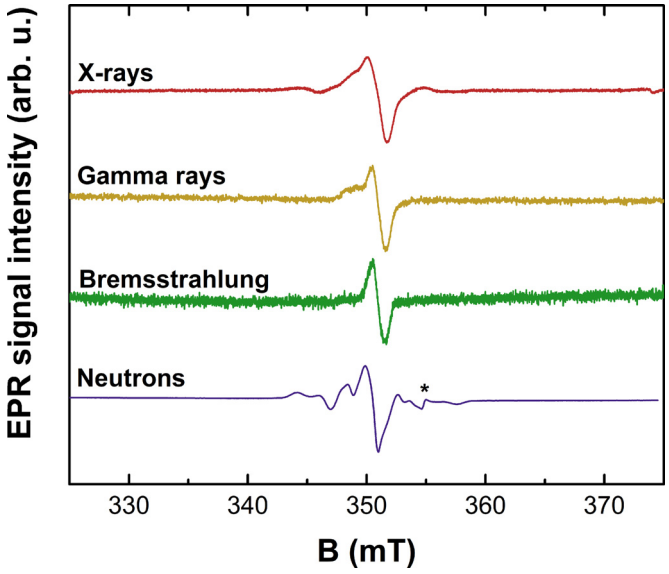

Fig. 1. X-band EPR spectra (0.2 mW microwave power) of the Li_4SiO_4 pebbles after irradiation with neutrons [19] and photons of different types and energies. The symbol "*" indicates the signal of the reference marker with $g = 1.9800 \pm 0.0005$.

Comparing the photon types and energies, EPR spectra with the best signal/noise ratio are obtained for the X-ray irradiated pebbles due to the feasibility of performing the measurements immediately after exposure to X-rays. It has been reported by Cipa et al. [28] that the $g = 2.00$ signal is not stable at ambient temperature, and the intensity of this signal decreases exponentially over time. Therefore, to analyse also the unstable radiation-induced defects, the X-ray irradiated pebbles were selected for further spectroscopic characterisation. In addition, the spectral shape is more similar to the neutron-irradiated pebbles. Despite the similarities, the EPR spectrum of the neutron-irradiated pebbles is highly structured and complicated due to significant differences in the interaction mechanisms, absorbed dose, and irradiation temperature (800–850 °C) in comparison to X-ray, gamma-ray, and *bremsstrahlung* irradiations at ambient temperature. However, spectral overlap of fewer signals can also be regarded as an advantage if contributions from several paramagnetic radiation-induced defects are to be distinguished and analysed. EPR spectra of the pebbles after irradiation with X-rays depending on microwave power are presented in Fig. 2.

EPR spectra dependence on microwave power strongly suggests that the overall spectrum is a superposition of signals from multiple radiation-induced defects. At high microwave power, the signal at 351 mT ($g = 2.00$) saturates and the spectrum shifts to 349 mT ($g = 2.01$). A similar effect has previously been demonstrated for the neutron-irradiated pebbles by Leys et al. [19]. In the 0.2-2 mW microwave power range, additional resonances at 325, 345, 356 and 374 mT are discernible.

A stepwise annealing experiment with consecutive EPR measurements after each step was carried out to investigate thermal stability of the radiation-induced defects; the results are shown in Fig. 3. The intensity and shape of the EPR spectra are strongly affected by the selected isochronal annealing temperature. The decrease of signal intensities upon increasing the annealing temperature is caused by thermally stimulated recombination processes of the accumulated radiation-induced defects. Analysis of double integral (DI) values of the EPR spectra in the 345-355 mT range reveals

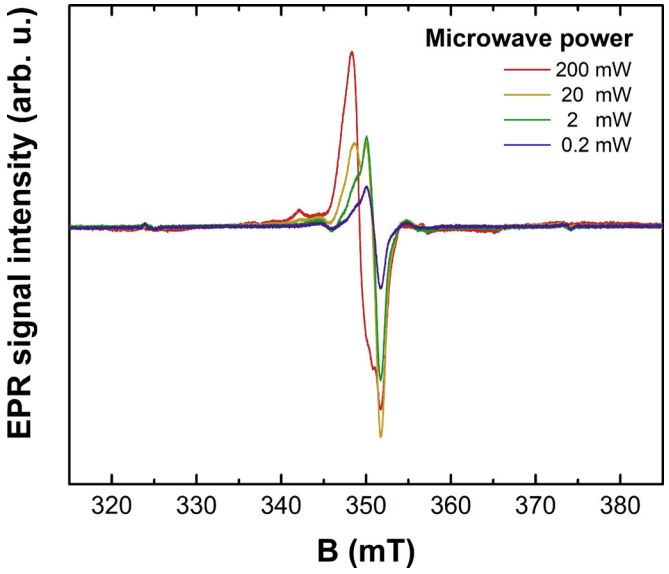

Fig. 2. X-band EPR spectra of the Li_4SiO_4 pebbles after irradiation with X-rays depending on microwave power.

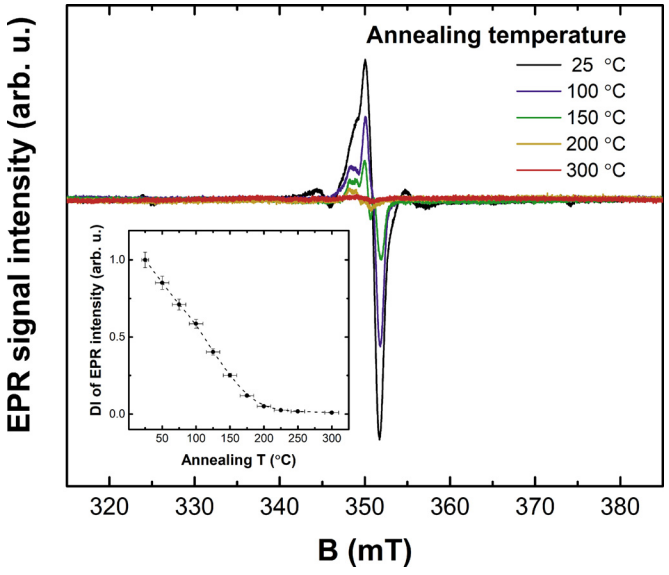

Fig. 3. X-band EPR spectra (2 mW microwave power) of the Li_4SiO_4 pebbles after irradiation with X-rays and subsequent isochronal annealing; inset: normalised double integral (DI) of EPR signal intensity in the 345–355 mT range as a function of annealing temperature.

two annealing stages which differ by the rate of the radiation-induced defect decay: 25–200 °C and 200–300 °C. Similar annealing behaviour of radiation-induced defects has been obtained in previous studies of irradiated lithium silicate materials [14,29,32]. The complicated evolution of signal shapes with annealing temperature corroborates that several radiation-induced defects contribute to the spectra.

It is advantageous to conduct EPR measurements at different experimental settings and perform spectra simulations to disentangle contributions of individual radiation-induced defects. The results of low-temperature EPR investigations are demonstrated in Fig. 4. The benefits of low-temperature EPR measurements are: (1) higher spectra intensities; (2) better resolved spectral features; and (3) a possibility to detect additional signals [34–37]. A point to be noted is a spectral shift towards lower magnetic field values due to a different microwave frequency (334 mT corresponds to $g = 2.00$).

The presence of at least two radiation-induced defects can be inferred from an inspection of the EPR spectra in Fig. 4(a). One is related to the feature at 334 mT ($g = 2.00$), which decreases in intensity as the acquisition temperature is lowered. The observation can be explained by the power saturation effect due to prolonged spin relaxation times at low temperature and high experimental microwave power [34]. The second signal, which is centred at 332 mT ($g = 2.01$), clearly exhibits a different temperature dependence. It reaches maximum intensity at 40 K and starts to saturate as the acquisition temperature is lowered to 10 K. This signal constitutes the dominant contribution to the spectrum acquired at ambient temperature and high microwave power (Fig. 2, 200 mW).

10 K was selected as the EPR spectra acquisition temperature for selective analysis of thermal properties of the $g = 2.01$ signal; the results are shown in Fig. 4(b). The signal is relatively stable in the 25-100 °C annealing range, but it decays rapidly if the temperature is increased to 150 °C. Spectra simulations were carried out for a precise determination of the g-factor with the following spin-Hamiltonian (SH):

$$H = g\mu_B BS \quad (1)$$

where g is the g-factor; μ_B – the Bohr magneton; B – external magnetic field; S – spin operator [34]. As the signal consists of a single resonance, its magnetic field position in the EPR spectrum can be uniquely characterised by the g-factor value. An excellent fit to the experimental spectrum was obtained with $S = ½$ and $g = 2.0120 \pm 0.0002$.

Unfortunately, not much else can be extracted from the low-temperature investigations; therefore, annealing behaviour is further analysed for the ambient temperature EPR spectra (Fig. 3). In order to disentangle the different signals contributing to the overall spectrum, spectra simulations are performed for the different annealing temperatures. As the EPR spectrum after annealing at 200 °C has been identified to originate from a single radiation-induced defect, it is selected as a starting point for simulations. Simulations of EPR spectra recorded at two microwave frequency bands are shown in Fig. 5. In the multifrequency EPR approach, the resolution of field-dependent interactions is enhanced, thus enabling a more precise determination of the g-factor [38]. In addition, the results are more unambiguous if a simultaneous fit for experimental spectra acquired at several microwave frequencies is achieved with the same parameter set [39,40]. The spectra in Fig. 5 correspond to the classical case of an $S = ½$ system with rhombic symmetry g-factor [34,40]; therefore, it has been labelled as "g_{rhombic}". SH (1) was used for simulations and the best fit was achieved with $g_1 = 2.0171 \pm 0.0005$, $g_2 = 2.0105 \pm 0.0005$ and $g_3 = 2.0009 \pm 0.0005$.

The low temperature-detected (Fig. 4) and g_{rhombic} (Fig. 5) EPR signals partially overlap and, hence, are problematic to analyse in conventional ambient temperature X-band measurements (Fig. 3). Due to a better resolution of slight differences of the g-factor at a higher microwave frequency, thermal annealing is additionally investigated at Q-band; the results are shown in Fig. 6. As established in the low-temperature EPR measurements (Fig. 4), a structureless component at $g = 2.012$ rapidly decreases in intensity after annealing above 100 °C. For the g_{rhombic} signal, some conclusions about the thermal properties can be inferred from the evolution of the spectral feature denoted by g_1. The signal exhibits an atypical annealing behaviour: it increases in intensity when heated in the 50-150 °C range and gradually decays in the 150–300 °C range.

The above-discussed signals bear striking resemblances to trapped hole centres (HC) in irradiated alkaline silicate glasses [41]. A hole centre which is delocalised over two non-bridging oxygen atoms bonded to the same silicon atom (HC_2) shares sev-

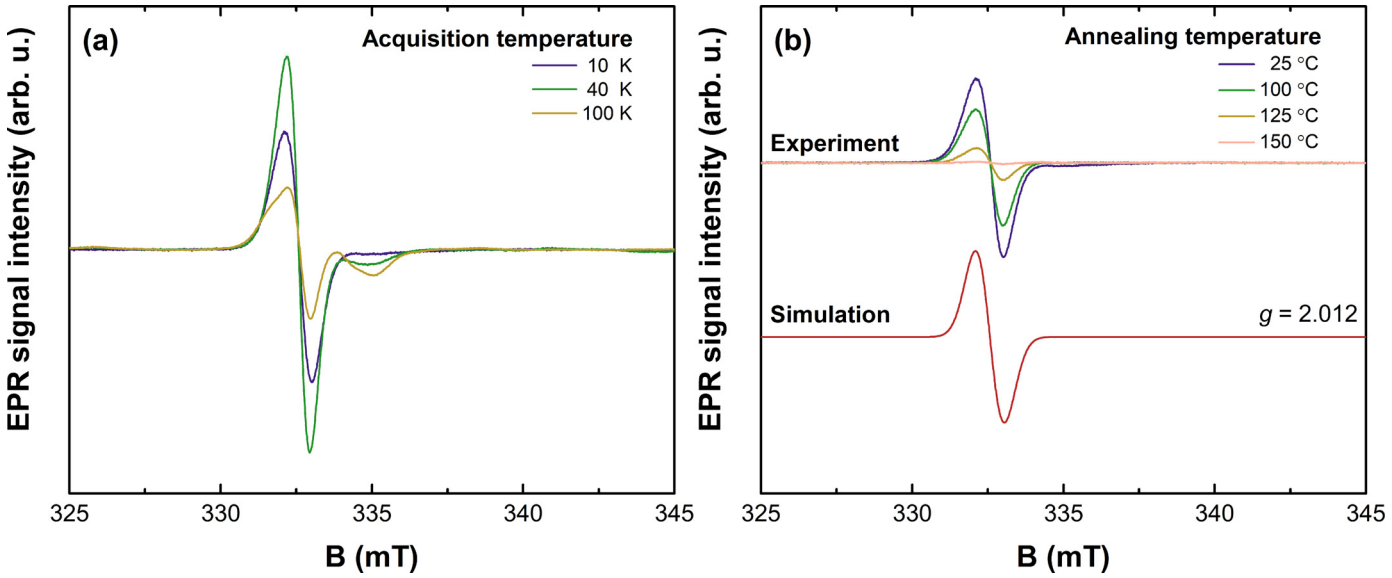

Fig. 4. X-band EPR spectra (20 mW microwave power) of the Li_4SiO_4 pebbles after irradiation with X-rays (a) at different spectra acquisition temperatures (10, 40 and 100 K) and (b) after subsequent sample isochronal annealing (acquired at 10 K).

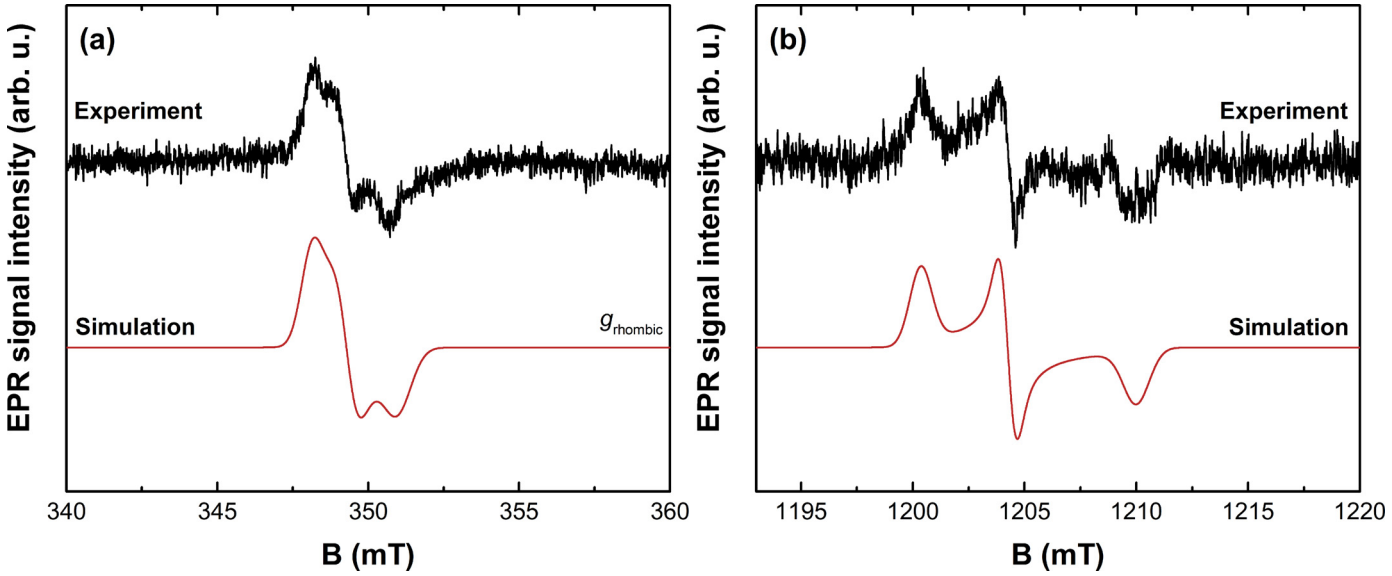

Fig. 5. Simulations of EPR spectra (10 mW microwave power) obtained at (a) X and (b) Q microwave frequency bands of the Li_4SiO_4 pebbles after irradiation with X-rays and subsequent annealing at 200 °C.

eral characteristics with the $g = 2.012$ signal: (1) favourable detection at high powers and low temperatures (Fig. 4); (2) a nearly isotropic g-factor near $g = 2.01$, although some anisotropy can be discerned from the Q-band measurements (Fig. 6); (3) disappearance of the signal above 150 °C (Figs. 4 and 6). If a hole is trapped on a single non-bridging oxygen atom (HC_1), the following similarities with the $g_{rhombic}$ signal are expected: (1) a more pronounced anisotropy of the g-factor with one of the components being close to $g_e = 2.0023$ (Fig. 5); (2) preferential detection after annealing above 150 °C (Figs. 5 and 6). Therefore, it seems reasonable to propose that the observed signals in the irradiated pebbles are the respective trapped HC counterparts ($g = 2.012$ – HC_2; $g_{rhombic}$ – HC_1). Highly overlapped EPR signals with similar shapes and parameters to the HC counterparts were also detected for the neutron-irradiated pebbles.

Afterwards, analysis was performed by going to lower annealing temperatures and including additional signals in order to achieve a fit between the experiment and simulations. The results for two annealing temperatures are demonstrated in Fig. 7.

Extra features besides the HC_1 signal are resolved in the EPR spectra of the irradiated pebbles annealed at lower temperatures. The experimental spectrum after annealing at 150 °C (Fig. 7(a)) can be simulated with the inclusion of two additional $S = ½$ systems with $g = 2.0046 \pm 0.0010$ and $g = 1.9986 \pm 0.0010$. To account for the spectral shape after annealing at 100 °C (Fig. 7(b)), a fourth $S = ½$ system with $g = 2.0015 \pm 0.0010$ must be included. Experimental spectra for the whole annealing range (Fig. 3) in the vicinity of 345–355 mT ($g = 2.00$) can satisfactorily be simulated by a combination of the identified signals. It needs to be highlighted that in the EPR spectrum of the neutron-irradiated pebbles, a complex signal with the g-factor at about 2.005 was observed, which can mainly be attributed to the more thermally stable $g = 2.0046$ signal detected here. One of the basic paramagnetic radiation-induced point defects in irradiated silicates is the

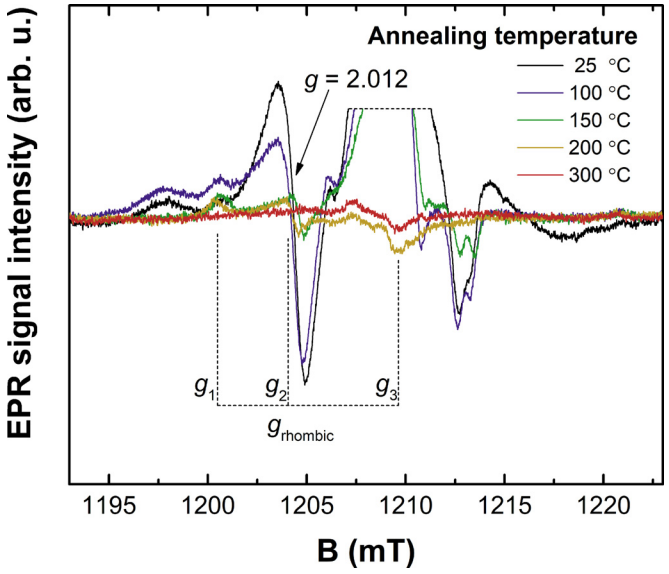

Fig. 6. Q-band EPR spectra (10 mW microwave power) of the Li_4SiO_4 pebbles after irradiation with X-rays and subsequent isochronal annealing.

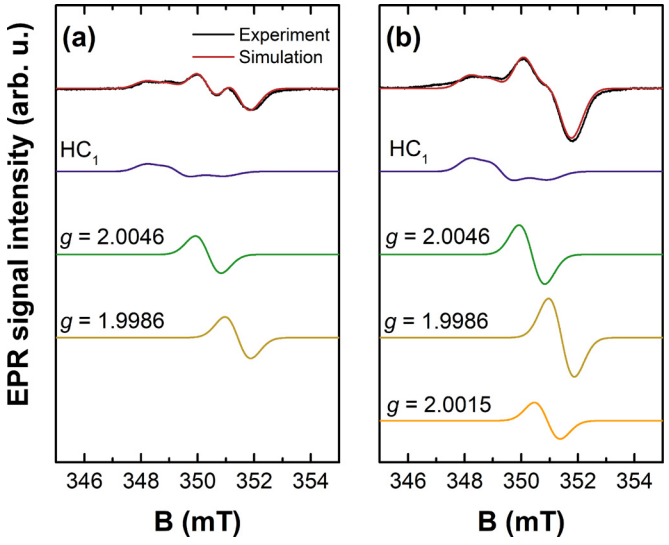

Fig. 7. Simulations of X-band EPR spectra (2 mW microwave power) of the Li_4SiO_4 pebbles after irradiation with X-rays and subsequent annealing at (a) 150 °C and (b) 100 °C.

E' centre. It occurs in different modifications with the reported g-factor values in the range of 2.000–2.002 in both crystalline and amorphous SiO_2 [42,43]; therefore, we propose that the $g = 2.0015$ signal originates from an E'-type centre. In the simplest case, the E'-type centre is described as an unpaired electron localised on a dandling tetrahedral (sp^3) orbital of a single silicon atom, which is bonded to three oxygen atoms in the crystalline lattice. The $g = 2.0046$ and $g = 1.9986$ signals could be associated with single electron paramagnetic centres, which are trapped at structural imperfections of the material.

Besides the composite $g = 2.00$ signal, several features occurring in a broader field range are also present. Analysis of the experimental spectrum prior to the annealing is provided in Fig. 8. The intensity of the 350 mT ($g = 2.00$) signal has been "cut-off" to highlight the additional signals.

A doublet with a separation of ~50 mT is characteristic to trapped atomic hydrogen (H^0) centres [40,44], which are formed due to the radiolysis of the chemisorption products of H_2O vapour

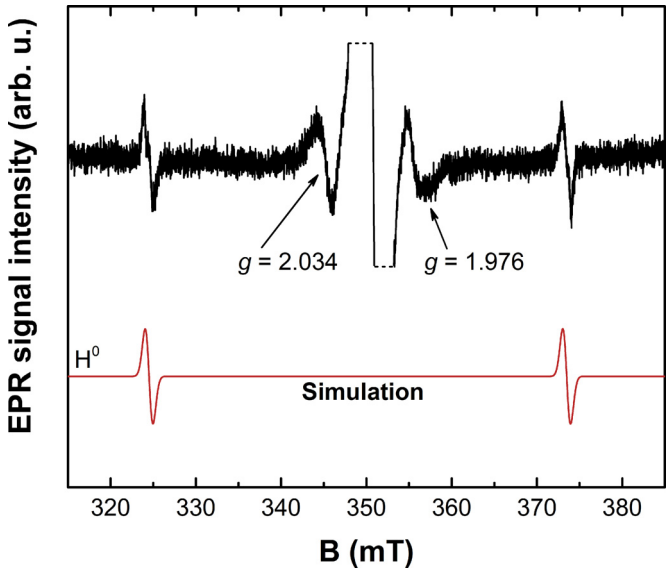

Fig. 8. X-band EPR spectrum (2 mW microwave power) of the Li_4SiO_4 pebbles after irradiation with X-rays prior to the isochronal annealing.

on the pebble surface [45]. The doublet originates from $S = ½$ hyperfine interaction with the nuclear spin $I = ½$ of the ^1H nucleus. Consequently, the following SH was employed for simulations:

$$H = g\mu_B BS + ASI \quad (2)$$

where A is the HF coupling tensor [34]. The fitted parameter values were $g = 2.0025 \pm 0.0010$ and $A = 1366 \pm 10$ MHz.

Analysis of the signals marked at $g = 2.034$ and $g = 1.976$ is hindered by the spectral overlap with the high-intensity $g = 2.00$ signal. Judging from the similarities in the microwave power dependence (Fig. 2) and annealing behaviour (Fig. 3), both features may as well originate from a single radiation-induced defect. EPR signals with similar g-factors and parameters were also detected for the neutron-irradiated pebbles. At the same time, the $g = 2.040$ and $g = 1.970$ signals were not detected in the pebbles after irradiation with photons of different types and energies. The detection of unstable radiation-induced defects with $g = 2.034$ and $g = 1.976$ signals in the neutron-irradiated pebbles could be explained by beta decay of the produced cobalt-60 isotope with a half-life of about 5.27 years and excited metastable nickel-60 nucleus emission of gamma rays during the storage stage after the HICU experiment, also called as self-irradiation. The neutron activation of the Li_4SiO_4 pebbles is strongly influenced by various micro-impurities [23].

An evaluation of the thermal stability of the identified radiation-induced defects in the pebbles after irradiation with photons of different types and energies is presented in Fig. 9. Annealing of the radiation-induced defects can be divided into four main stages. The least stable radiation-induced defects, namely the H^0 centre and the defect(s) associated with $g = 2.034$ and $g = 1.976$ signals, decay rapidly in the 50–100 °C annealing range. The second group of radiation-induced defects (HC_2; defect associated with the $g = 2.0015$ signal, possibly an E'-type centre) is destroyed after annealing at 150 °C. It should be noted that it was possible to monitor the evolution of the HC_2 signal reliably for the whole annealing range due to the selective excitation at low temperature (Fig. 4); however, analysis of the $g = 2.0015$ signal below 100 °C was problematic. During the third stage (100–200 °C) a correlated decay of the $g = 1.9986$ and $g = 2.0046$ signals (Fig. 7) is observed. Finally, the HC_1 signal (Figs. 5 and 6) exhibits the highest thermal stability and is completely annihilated above 300 °C. A comparison of Fig. 9 and the inset of Fig. 3 suggests that the

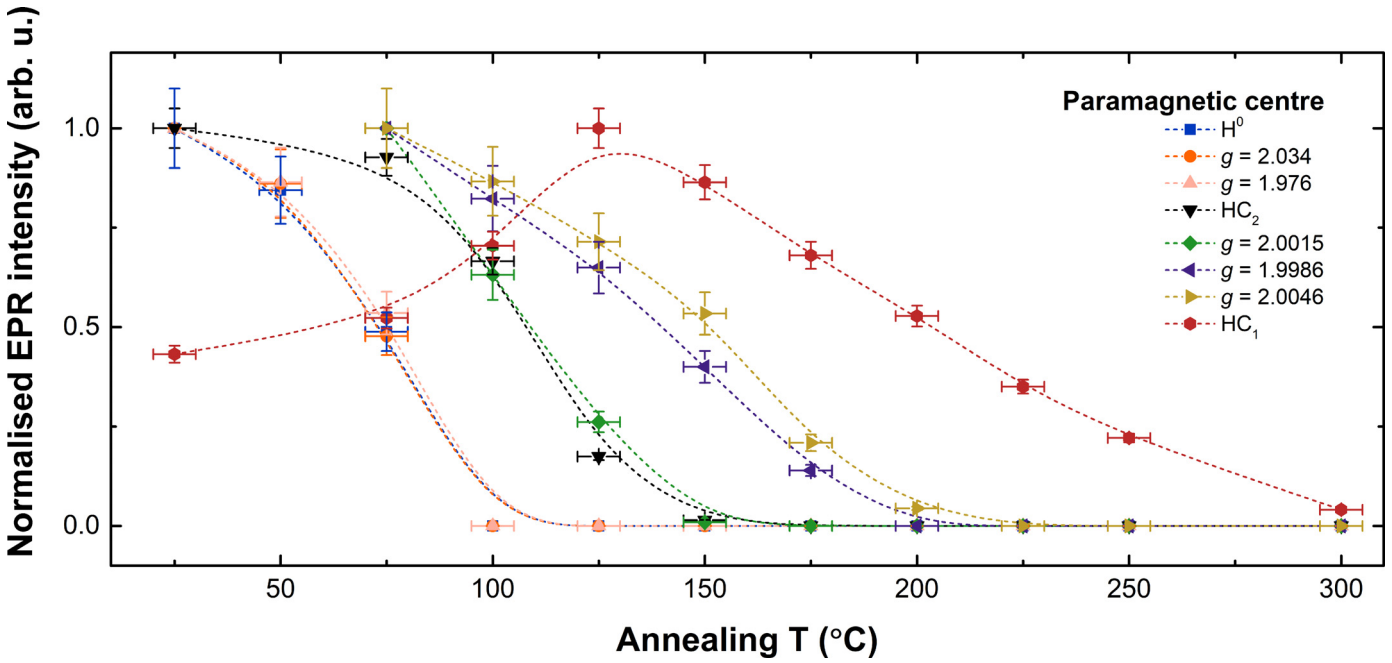

Fig. 9. Decay of radiation-induced defects with temperature in the Li_4SiO_4 pebbles after irradiation with photons of different types and energies; normalised representation.

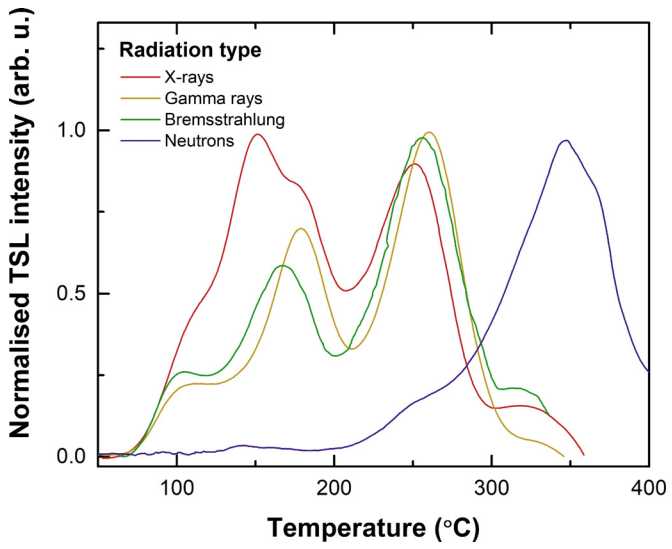

Fig. 10. Normalised TSL glow curves (β = 2 °C s^{-1}) of the Li_4SiO_4 pebbles after irradiation with neutrons [19] and photons of different types and energies.

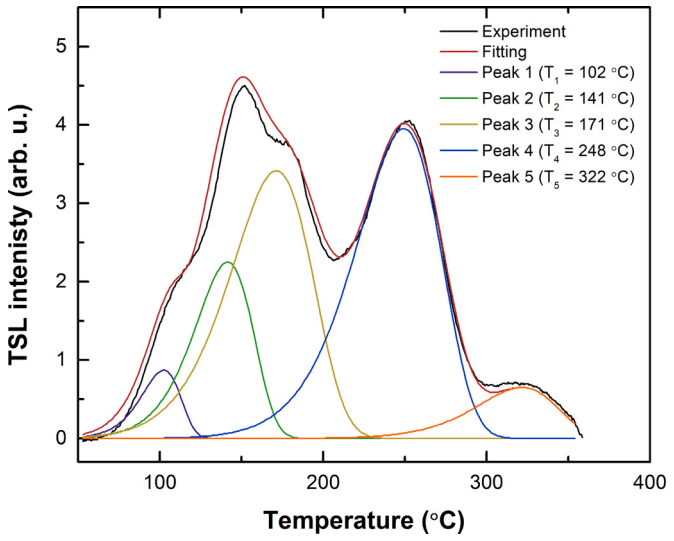

Fig. 11. Deconvoluted TSL glow curve (β = 2 °C s^{-1}) of the Li_4SiO_4 pebbles after irradiation with X-rays.

latter process is responsible for the "slow" defect decay in the 200-300 °C range, while the "fast" decay (50-200 °C) is a complex process involving multiple radiation-induced defects. Suzuki et al. [46] and Osuo et al. [47] reported possible conversion reactions of the E'-centres to non-bridging oxygen hole centres and further to peroxide radicals, which may occur during the annealing.

3.2. Thermally stimulated luminescence (TSL)

To acquire additional information about thermal properties and the EPR simulation data of the formed and accumulated paramagnetic radiation-induced defects, TSL glow curves and spectra of the photon-irradiated Li_4SiO_4 pebbles were obtained. TSL glow curves of the pebbles after irradiation with neutrons and photons of different types and energies are shown in Fig. 10. The primary effect leading to the creation of a TSL glow peak is thermal stimulation of the electrons and holes which are trapped at intrinsic and extrinsic defects of the pebbles during irradiation. As described previously, the content of metal impurities in the analysed pebbles is negligible; therefore, it is expected that all trapping processes are mainly determined by intrinsic defects. A linear increase in the temperature of the irradiated pebbles causes a gradual release of the trapped electrons and/or holes inducing subsequent recombination at luminescence centres. The relaxation of the luminescence centre from the excited state to the ground state is accompanied by the emission of light with specific energy (E_{em}) and wavelength (λ_{em}). The temperature maxima (T_m) of TSL glow peaks depend on the heating rate (β) and are shifted towards higher temperatures when the heating rate is increased [48]. The TSL glow curves of the photon-irradiated pebbles are complex and consist of several overlapped peaks with temperature maxima between 50 °C and 400 °C indicating different trapping sites with various depths. Similar TSL

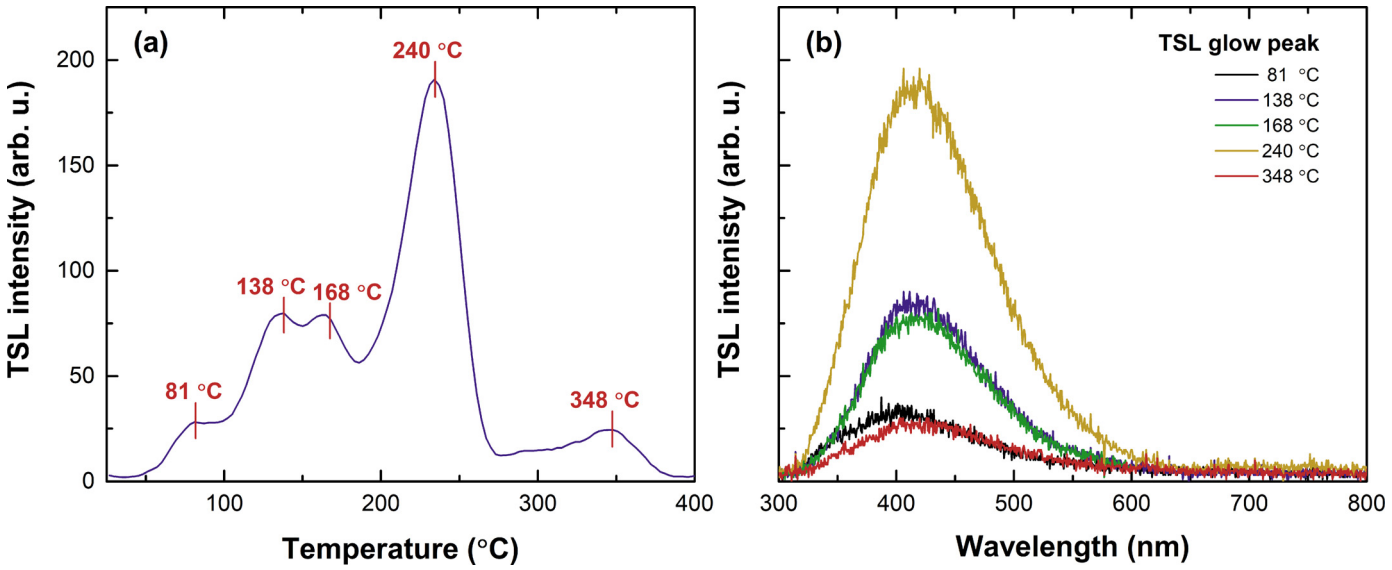

Fig. 12. TSL glow curve and spectra of the Li_4SiO_4 pebbles after irradiation with X-rays ($\beta = 1$ °C s^{-1}): (a) intensity of the luminescence band with a wavelength at about 420 nm depending on temperature; (b) wavelength-based spectra of the five most pronounced glow peaks.

glow curves were also observed in the studies by Cipa et al. [28], Feldbach et al. [49], Leys et al. [19], and Abramenkovs et al. [50]. In the neutron-irradiated pebbles, mainly the high-temperature peaks above 300 °C were detected, which can be related to thermally stimulated recombination processes of the formed thermally stable complex electron type centres: radiation-induced defect aggregates, for example, F_n centres, or radiolysis products, for example, small Li_n particles with a size below 1 μm [30,33]. At least three highly overlapping peaks with temperature maxima at about 340, 370 and 390 °C were distinguished [19]. Peaks with a temperature maximum below 300 °C, which can be attributed to simple electron type centres with low and medium trap depths, were practically not observed due to an elevated irradiation temperature in the HICU experiment.

The deconvoluted peaks in the TSL glow curve of the pebbles after irradiation with X-rays are shown in Fig. 11. TSL glow curves were separated into five first-order kinetic peaks with maxima temperatures at about 100, 140, 170, 250 and 320 °C. The obtained results correlate with the EPR simulation data for the "fast" and "slow" decay processes of the paramagnetic radiation-induced defects (Figs. 3 and 9). Nevertheless, it is possible that not all formed and accumulated radiation-induced defects have paramagnetic properties necessary for the detection of EPR or participate in radiative recombination processes necessary for the detection of TSL. On the basis of the obtained results of isochronal annealing, the first peak at about 100 °C can be related to the decay of the defect(s) associated with $g = 2.034$ and $g = 1.976$ signals, while the second and third peaks at about 140 and 170 °C with the decay of HC_2 and the defect associated with $g = 2.0015$ signal. The fourth peak at about 250 °C can be related to the decay of the defects associated with $g = 1.9986$ and $g = 2.0046$ signals, and probably HC_1. The fifth peak at about 320 °C can be related to the annihilation of HC_1 and a nonparamagnetic radiation-induced defect with a high trap depth.

TSL glow curve and spectra of the pebbles after irradiation with X-rays are shown in Fig. 12. In this case, it needs to be highlighted that the heating rate is smaller; therefore, all peaks are slightly shifted to lower temperatures. The intensity of the luminescence band with a wavelength at about 420 nm depending on temperature can be seen in Fig. 12(a), whereas wavelength-based spectra of the five most pronounced peaks are shown in Fig. 12(b). Fitting of the converted and normalised energy-based spectra for the TSL glow peaks with maximum temperatures at about 78 °C, 240 °C, and 348 °C is shown in Fig. 13. At least three gaussian bands with energy maxima at about 2.99 eV, 2.88 eV, and 2.85 eV were distinguished, which can indicate that there are several luminescence centres. However, judging from the similarities of the maxima positions and bandwidths, the variations of the luminescence signals at different temperatures could as well be explained by a single luminescence centre with slight variations in its local structure [51]. The first band at 2.99 eV is detected at temperatures below 100 °C, the second band at 2.88 eV is observed in the temperature range from 100 °C to 270 °C, while the third band at 2.85 eV is measured at a temperature above 270 °C. Previously, similar bands were detected in the *in-situ* and *ex-situ* luminescence studies by Cipa et al. [28], Feldbach et al. [49], and Moritani et al. [52]. On the basis of EPR and TSL analysis of the obtained isochronal annealing results, the formation of a band with 2.99 eV can be related to electron-hole recombination processes of the unstable paramagnetic radiation-induced defect(s) associated with the $g = 2.034$ and $g = 1.976$ signals. The formation of bands in the 2.85-2.88 eV range can be related to the thermally stimulated recombination processes of the variously trapped electrons and paramagnetic hole type radiation-induced defects, for example, HC_2 and HC_1.

A summary of the obtained simulation and deconvolution data for EPR and TSL measurements for the pebbles after irradiation with photons of different types and energies is provided in Table 1. The thermally stimulated decay of the paramagnetic radiation-induced defects can be divided into four main stages and correlated with temperature maxima and luminescence energy of radiative recombination processes.

The obtained results of EPR and TSL analyses for individual paramagnetic radiation-induced defects in the photon-irradiated pebbles have a good resemblance to the neutron-irradiated pebbles from the HICU experiment. However, due to a complex interaction mechanism, a higher absorbed dose, and an elevated irradiation temperature, it is expected that the formation of thermally stable radiation-induced defect aggregates and radiolysis products dominated in the pebbles during irradiation with neutrons. In ad-

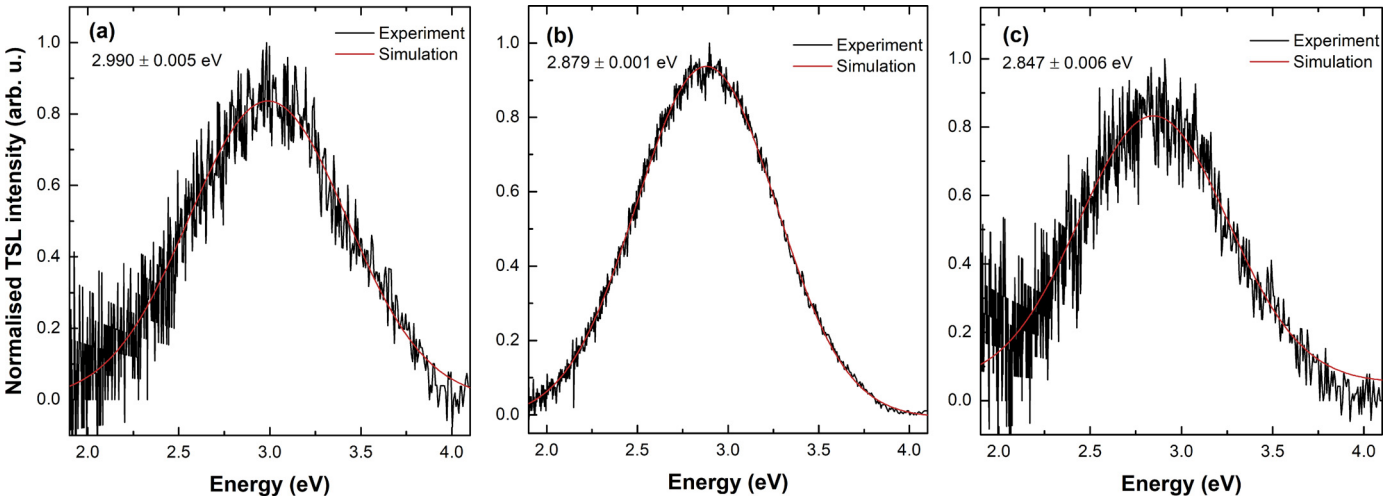

Fig. 13. Fitting of converted and normalised energy-based TSL spectra for the glow peak with the maximum at about (a) 78 °C, (b) 240 °C, and (c) 348 °C of the Li_4SiO_4 pebbles after irradiation with X-rays.

Table 1
A summary of thermal properties of radiation-induced defects in the Li_4SiO_4 pebbles after irradiation with photons of different types and energies.

Stage	I	II	III	IV
Annealing temperature	<100 °C	100–150 °C	150–200 °C	>200 °C
Paramagnetic radiation-induced defects	Decay of the H^0 centre and the defect(s) associated with $g = 2.034$ and $g = 1.976$ signals	$HC_2 \rightarrow HC_1$ transition; decay of HC_2 and the defect associated with $g = 2.0015$ signal	Decay of the defects associated with $g = 1.9986$ and $g = 2.0046$ signals, and probably HC_1	Annihilation of HC_1
Radiative recombination processes	$T_1 = 100$ °C** $E_{em} = 2.99$ eV	$T_2 = 140$ °C $T_3 = 170$ °C $E_{em} = 2.89$ eV	$T_4 = 250$ °C $E_{em} = 2.88$ eV	$T_{5\text{-}7} = 300\text{-}400$ °C $E_{em} = 2.85$ eV

** $\beta = 2$ °C s^{-1}.

dition, not all formed and accumulated radiation-induced defect aggregates and radiolysis products have paramagnetic properties or participate in radiative recombination processes, limiting detection by EPR and TSL spectroscopy techniques. Nevertheless, the tritium release behaviour for the neutron-irradiated pebbles correlates with the thermally stimulated decay of the paramagnetic radiation-induced defects, and it starts at about 200 °C [18,19]. Tritium is released as partially tritiated water HTO, HT and corresponding fragments.

The data reported herein represent the most comprehensive comparative analysis of thermal properties of paramagnetic radiation-induced defects in irradiated Li_4SiO_4 containing breeder material up to date. The acquired knowledge base about the local structure and stability of the different types of radiation-induced defects will be indispensable to better characterise the correlation between recombination processes of the defects and tritium release, thus enabling to develop a new generation of materials for thermonuclear fusion reactors.

4. Conclusions

In this research, novel insights into the individual structure, electronic configuration, and thermal stability of paramagnetic radiation-induced defects in photon-irradiated Li_4SiO_4 containing breeder material have been obtained via correlated EPR and TSL measurements, glow curve and spectra deconvolution into individual components and simulations. At least seven paramagnetic radiation-induced defects are generated after exposure of the Li_4SiO_4 pebbles with a surplus of SiO_2 to photons of different types and energies: X-rays with an energy up to 45 keV, gamma rays with an average energy of 1.25 MeV, and *bremsstrahlung* with an energy up to 6 MeV. All of the detected EPR signals can be attributed to spin $S = ½$ systems with distinct g-factor values and thermal characteristics. The annihilation of the radiation-induced defects occurs in four main stages: (1) <100 °C (H^0 centres and the defect(s) associated with the $g = 2.034$ and $g = 1.976$ signals); (2) 100-150 °C (HC_2 and the defect associated with the $g = 2.0015$ signal); (3) 150-200 °C (the defects associated with the $g = 1.9986$ and $g = 2.0046$ signals, and probably HC_1) and (4) >200 °C (HC_1). Annealing of the radiation-induced defects with a linear increase in the temperature up to 400 °C is accompanied by luminescence centred at about 2.99 eV, 2.88 eV, and 2.85 eV. The peaks of TSL glow curves are well-correlated with radiation-induced defect decay kinetics. However, the acquired results also clearly demonstrate that not all formed and accumulated radiation-induced defects have paramagnetic properties.

The simulation and deconvolution data of EPR spectra, TSL glow curves and spectra are in good agreement with the results, which have been acquired for the neutron-irradiated pebbles from the HICU experiment. However, not all radiation-induced defects were detected in the photon-irradiated pebbles in comparison to the neutron-irradiated pebbles, due to a complex neutron interaction mechanism, a higher absorbed dose, and an elevated irradiation temperature.

Declaration of Competing Interest

The authors declare that they have no known competing financial interests or personal relationships that could have appeared to influence the work reported in this paper.

CRediT authorship contribution statement

Andris Antuzevics: Conceptualization, Methodology, Validation, Formal analysis, Investigation, Writing – original draft, Writing – review & editing, Visualization. **Arturs Zarins:** Conceptualization, Methodology, Validation, Formal analysis, Investigation, Writing – original draft, Writing – review & editing, Visualization, Funding acquisition. **Anna Ansone:** Methodology, Formal analysis, Investigation, Writing – review & editing. **Janis Cipa:** Methodology, Formal analysis, Investigation, Writing – review & editing. **Gunta Kizane:** Conceptualization, Writing – review & editing, Resources, Supervision, Project administration. **Julia M. Leys:** Conceptualization, Resources, Writing – review & editing. **Regina Knitter:** Conceptualization, Resources, Writing – review & editing.

Acknowledgments

This study has been performed within the framework of the Latvian-Ukrainian cooperation program project (agreement No. LV-UA/2021/4) and the European Regional Development Fund (ERDF) project (application No. 1.1.1.2/VIAA/4/20/614). Institute of Solid State Physics, University of Latvia as the Centre of Excellence has received funding from the European Union's Horizon 2020 Framework Programme H2020-WIDESPREAD-01-2016-2017-TeamingPhase2 under grant agreement No. 739508, project CAMART².

References

[1] J.M. Heuser, M.H.H. Kolb, T. Bergfeldt, R. Knitter, Long-term thermal stability of two-phased lithium orthosilicate/metatitanate ceramics, J. Nucl. Mater. 507 (2018) 396–402, doi:10.1016/j.jnucmat.2018.05.010.

[2] Q. Zhou, A. Togari, M. Nakata, M. Zhao, F. Sun, Q. Xu, Y. Oya, Release kinetics of tritium generation in neutron irradiated biphasic Li_2TiO_3–Li_4SiO_4 ceramic breeder, J. Nucl. Mater. 522 (2019) 286–293, doi:10.1016/j.jnucmat.2019.05.033.

[3] J. Zhou, Q. Wang, S. Li, H. Li, Q. Zhou, Phase composition control of biphasic tritium breeding ceramics and correlation behavior of lithium and tritium, J. Nucl. Mater. 557 (2021) 153294, doi:10.1016/j.jnucmat.2021.153294.

[4] J. Yan, N. He, X. Chen, C. Xiao, L.J. Zhao, T. Gao, Design, synthesis and characterization of advanced tritium breeder: $Li_4Si_{1-x}Ti_xO_4$ ceramics, Ceram. Int. 47 (2021) 14178–14182, doi:10.1016/j.ceramint.2021.02.004.

[5] Y. Gong, J. Li, S. Yang, M. Yang, H. Dang, Y. Ren, G. Zhang, T. Lu, Improvement of crushing strength and thermal conductivity by introduction of hetero-element Al into Li_4SiO_4, Ceram. Int. 45 (2019) 24564–24569, doi:10.1016/j.ceramint.2019.08.185.

[6] O. Leys, M.H.H. Kolb, A. Pucci, R. Knitter, Study of lithium germanate additions to advanced ceramic breeder pebbles, J. Nucl. Mater. 518 (2019) 234–240, doi:10.1016/j.jnucmat.2019.03.010.

[7] M. Xiang, J. Zheng, S. Li, C. Hu, J. Cui, Y. Zhang, Q. Qi, F. Yue, Preparation of coated Li_2TiO_3 and Li_4SiO_4 pebbles by fluidized bed chemical vapor deposition for advanced tritium breeders, Fus. Eng. Des. 165 (2021) 112245, doi:10.1016/j.fusengdes.2021.112245.

[8] M. Zmitko, P. Vladimirov, R. Knitter, M. Kolb, O. Leys, J. Heuser, H.C. Schneider, R. Rolli, V. Chakin, S. Pupeschi, L. Magielsen, A. Fedorov, Y. Poitevin, Development and qualification of functional materials for the European HCPB TBM, Fus. Eng. Des. 136 (2018) 1376–1385, doi:10.1016/j.fusengdes.2018.05.014.

[9] N. Baluc, Materials for fusion power reactors, Plasma Phys. Control. Fus. 48 (2006) B165–B177, doi:10.1088/0741-3335/48/12B/S16.

[10] L.W. Hobbs, F.W. Clinard, S.J. Zinkle, R.C. Ewing, Radiation effects in ceramics, J. Nucl. Mater. 216 (1994) 291–321, doi:10.1016/0022-3115(94)90017-5.

[11] Y. Shi, T. Lu, T. Gao, X. Xiang, Y. Gong, M. Yang, L. Feng, H. Wang, C. Dang, First principle study of tritium trapping at oxygen vacancies in Li_4SiO_4, J. Nucl. Mater. 508 (2018) 257–264, doi:10.1016/j.jnucmat.2018.05.055.

[12] Y. Shi, T. Lu, T. Gao, X. Xiang, Q. Zhang, X. Yu, Y. Gong, M. Yang, Density functional study of lithium vacancy in Li_4SiO_4: trapping of tritium and helium, J. Nucl. Mater. 467 (2015) 519–526, doi:10.1016/j.jnucmat.2015.09.017.

[13] R. Zhang, L. Wan, H. Xiao, J. Wang, C. Xiao, X. Chen, T. Gao, Ab initio study of helium in Li_4SiO_4 crystals: electronic properties, migration, and vacancy capture mechanism, Ceram. Int. 47 (2021) 20239–20247, doi:10.1016/j.ceramint.2021.04.031.

[14] Y. Nishikawa, M. Oyaidzu, A. Yoshikawa, K. Munakata, M. Okada, M. Nishikawa, K. Okuno, Correlation between tritium release and thermal annealing of irradiation damage in neutron-irradiated Li_2SiO_3, J. Nucl. Mater. 367–370 (2007) 1371–1376, doi:10.1016/j.jnucmat.2007.03.251.

[15] J. Ba, R. Zeng, X. Yan, R. Li, W. Wu, F. Li, X. Xiang, D. Meng, T. Tang, Long-term helium bubble evolution in sequential He^+ and H^+ irradiated Li_4SiO_4, Ceram. Int. 47 (2021) 32310–32317, doi:10.1016/j.ceramint.2021.08.126.

[16] J.B.J. Hegeman, E.D.L. van Essen, M. Jong, J.G. van der Laan, J. Reimann, Thermomechanical behaviour of ceramic breeder pebble stacks for HICU, Fus. Eng. Des. 69 (2003) 425–429, doi:10.1016/S0920-3796(03)00086-3.

[17] M.H.H. Kolb, J.M. Heuser, R. Rolli, H.C. Schneider, R. Knitter, M. Zmitko, The HICU PIE results of EU ceramic breeder pebbles: general characterization, J. Nucl. Mater. 531 (2020) 152023, doi:10.1016/j.jnucmat.2020.152023.

[18] J.M. Heuser, M.H.H. Kolb, R. Rolli, H.C. Schneider, R. Knitter, M. Zmitko, The HICU PIE results of EU ceramic breeder pebbles: tritium release properties, J. Nucl. Mater. 531 (2020) 152024, doi:10.1016/j.jnucmat.2020.152024.

[19] J.M. Leys, A. Zarins, J. Cipa, L. Baumane, G. Kizane, R. Knitter, Radiation-induced effects in neutron- and electron-irradiated lithium silicate ceramic breeder pebbles, J. Nucl. Mater. 540 (2020) 152347, doi:10.1016/j.jnucmat.2020.152347.

[20] J.E. Tiliks, G.K. Kizane, A.A. Supe, A.A. Abramenkovs, J.J. Tiliks, V.G. Vasiljev, Formation and properties of radiation-induced defects and radiolysis products in lithium orthosilicate, Fus. Eng. Des. 17 (1991) 17–20, doi:10.1016/0920-3796(91)90029-P.

[21] A. Zarins, O. Valtenbergs, G. Kizane, A. Supe, R. Knitter, M.H.H. Kolb, O. Leys, L. Baumane, D. Conka, Formation and accumulation of radiation-induced defects and radiolysis products in modified lithium orthosilicate pebbles with additions of titanium dioxide, J. Nucl. Mater. 470 (2016) 187–196, doi:10.1016/j.jnucmat.2015.12.027.

[22] R. Knitter, B. Alma, G. Roth, Crystallisation and microstructure of lithium orthosilicate pebbles, J. Nucl. Mater. 367–370 (2007) 1387–1392, doi:10.1016/j.jnucmat.2007.04.002.

[23] R. Knitter, U. Fischer, S. Herber, C. Adelhelm, Reduction of impurities and activation of lithium orthosilicate breeder materials, J. Nucl. Mater. 386–388 (2009) 1071–1073, doi:10.1016/j.jnucmat.2008.12.284.

[24] S. Stoll, CW-EPR spectral simulations: solid state, Methods Enzymol. 563 (2015) 121–142, doi:10.1016/bs.mie.2015.06.003.

[25] G. Kizane, J. Tiliks, A. Vitins, J. Rudzitis, Tritium localisation and release from the ceramic pebbles of breeder, J. Nucl. Mater. 329–333 (2004) 1287–1290, doi:10.1016/j.jnucmat.2004.04.229.

[26] M. Puchalska, P. Bilski, GlowFit—a new tool for thermoluminescence glow-curve deconvolution, Radiat. Meas. 41 (2006) 659–664, doi:10.1016/j.radmeas.2006.03.008.

[27] Y. Wang, P.D. Townsen, Common mistakes in luminescence analysis, J. Phys. Conf. Ser. 398 (2012) 012003, doi:10.1088/1742-6596/398/1/012003.

[28] J. Cipa, A. Zarins, A. Supe, G. Kizane, A. Zolotarjovs, L. Baumane, L. Trinkler, O. Leys, R. Knitter, X-ray induced defects in advanced lithium orthosilicate pebbles with additions of lithium metatitanate, Fus. Eng. Des. 143 (2019) 10–15, doi:10.1016/j.fusengdes.2019.03.096.

[29] G. Ran, C. Xiao, X. Chen, Y. Gong, L. Zhao, H. Wang, X. Wang, Annihilation behavior of irradiation defects in Li_4SiO_4 irradiated with high thermal neutron fluence, J. Nucl. Mater. 491 (2017) 43–47, doi:10.1016/j.jnucmat.2017.04.055.

[30] A. Zarins, O. Leys, G. Kizane, A. Supe, L. Baumane, M. Gonzalez, V. Correcher, C. Boronat, A. Zolotarjovs, R. Knitter, Behaviour of advanced tritium breeder pebbles under simultaneous action of accelerated electrons and high temperature, Fus. Eng. Des. 121 (2017) 167–173, doi:10.1016/j.fusengdes.2017.06.033.

[31] J.M. Heuser, A. Zarins, L. Baumane, G. Kizane, R. Knitter, Radiation stability of long-term annealed bi-phasic advanced ceramic breeder pebbles, Fus. Eng. Des. 138 (2019) 395–399, doi:10.1016/j.fusengdes.2018.12.034.

[32] B. Ji, S. Gu, Q. Qi, X.-C. Li, Y. Zhang, H. Zhou, G.N. Luo, Annihilation kinetics of irradiation defects in promising tritium breeding pebbles, Nucl. Mater. Energy 27 (2021) 101015, doi:10.1016/j.nme.2021.101015.

[33] J. Tīliks, G. Ķizāne, A. Vitiņš, Ģ. Vītiņš, J. Meistars, Physicochemical processes in blanket ceramic materials, Fus. Eng. Des. 69 (2003) 519–522, doi:10.1016/S0920-3796(03)00120-0.

[34] J.A. Weil, J.R. Bolton, Electron Paramagnetic Resonance, Wiley, 2007.

[35] A. Laurikenas, D. Sakalauskas, A. Marsalka, R. Raudonis, A. Antuzevics, V. Balevicius, A. Zarkov, A. Kareiva, Investigation of lanthanum substitution effects in yttrium aluminium garnet: importance of solid state NMR and EPR methods, J. Sol Gel Sci. Technol. 97 (2021) 479–487, doi:10.1007/s10971-020-05445-2.

[36] A. Antuzevics, EPR characterization of erbium in glasses and glass ceramics, Low Temp. Phys. 46 (2020) 1149–1153, doi:10.1063/10.0002465.

[37] N. Mironova-Ulmane, A.I. Popov, G. Krieke, A. Antuzevics, V. Skvortsova, E. Elsts, A. Sarakovskis, Low-temperature studies of Cr^{3+} ions in natural and neutron-irradiated g-Al spinel, Low Temp. Phys. 46 (2020) 1154–1159, doi:10.1063/10.0002467.

[38] S.K. Misra, Multifrequency Electron Paramagnetic Resonance: Theory and Applications, Wiley, 2011, doi:10.1002/9783527633531.

[39] D.V. Shurtakova, B.V. Yavkin, G.V. Mamin, S.B. Orlinskii, V.P. Sirotinkin, A.Y. Fedotov, A. Shinkarev, A. Antuzevics, I.V. Smirnov, V.I. Tovtin, E.E. Starostin, M.R. Gafurov, V.S. Komlev, X-ray diffraction and multifrequency EPR study of radiation-induced room temperature stable radicals in octacalcium phosphate, Radiat. Res. 195 (2021), doi:10.1667/RADE-20-00194.1.

[40] G. Krieke, A. Antuzevics, B. Berzina, Defect formation in photochromic Ca_2SnO_4: Al^{3+}, Mater. Today Commun. 28 (2021) 102592, doi:10.1016/j.mtcomm.2021.102592.

[41] D.L. Griscom, Electron spin resonance studies of trapped hole centers in irradiated alkali silicate glasses: a critical comment on current models for HC_1 and HC_2, J. Non Cryst. Solids 64 (1984) 229–247, doi:10.1016/0022-3093(84)90220-5.

[42] R.I. Mashkovtsev, Y. Pan, Nature of paramagnetic defects in α-quartz: progresses in the first decade of the 21st century, in: B. Novak, P. Marek (Eds.), New Developments in Quartz Research: Varieties, Crystal Chemistry and Uses in Technology Chapter: 2., Nova Science, 2013, pp. 65–104.

[43] A. Alessi, S. Agnello, G. Buscarino, Y. Pan, R.I. Mashkovtsev, EPR on radiation-induced defects in SiO_2, Appl. EPR Radiat. Res. (2014) 255–295, doi:10.1007/978-3-319-09216-4_7.
[44] S. Stoll, A. Ozarowski, R.D. Britt, A. Angerhofer, Atomic hydrogen as high-precision field standard for high-field EPR, J. Magn. Reson. 207 (2010) 158–163, doi:10.1016/j.jmr.2010.08.006.
[45] A. Zarins, G. Kizane, A. Supe, R. Knitter, M.H.H. Kolb, J. Tiliks, L. Baumane, Influence of chemisorption products of carbon dioxide and water vapour on radiolysis of tritium breeder, Fus. Eng. Des. 89 (2014) 1426–1430, doi:10.1016/j.fusengdes.2014.01.005.
[46] S. Suzuki, M. Kobayashi, R. Kurata, W. Wang, T. Fujii, H. Yamana, K. Feng, Y. Oya, K. Okuno, Elucidation of annihilation processes of defects induced by γ-irradiation in Li_2TiO_3, Fus. Eng. Des. 85 (2010) 2331–2333, doi:10.1016/j.fusengdes.2010.09.022.
[47] J. Osuo, M. Kobayashi, R. Kurata, A. Hamada, W. Wang, T. Fujii, H. Yamana, T. Luo, K. Feng, Y. Oya, K. Okuno, Dependence of gamma-ray dose on annihilation processes of irradiation defects in Li_2TiO_3, Fus. Eng. Des. 86 (2011) 2362–2364, doi:10.1016/j.fusengdes.2011.04.080.
[48] A.J.J. Bos, Thermoluminescence as a research tool to investigate luminescence mechanisms, Materials 10 (2017) 1357, doi:10.3390/ma10121357.
[49] E. Feldbach, A. Kotlov, I. Kudryavtseva, P. Liblik, A. Lushchik, A. Maaroos, I. Martinson, V. Nagirnyi, E. Vasil'chenko, Low-temperature irradiation effects in lithium orthosilicates, Nucl. Instrum. Methods Phys. Res. Sect. B Beam Interact. Mater. Atoms 250 (2006) 159–163, doi:10.1016/j.nimb.2006.04.100.
[50] A. Abramenkovs, E. Kaschejva, V. Grishmanovs, S. Tanaka, Thermoluminescence study of irradiated lithium orthosilicate, Fus. Eng. Des. 39–40 (1998) 693–697, doi:10.1016/S0920-3796(98)00247-6.
[51] Y.X. Pan, W. Wang, G.K. Liu, S. Skanthakumar, R.A. Rosenberg, X.Z. Guo, K.K. Li, Correlation between structure variation and luminescence red shift in YAG:Ce, J. Alloy. Compd. 488 (2009) 638–642, doi:10.1016/j.jallcom.2009.04.082.
[52] K. Moritani, S. Tanaka, H. Moriyama, Production behavior of irradiation defects in lithium silicates and silica under ion beam irradiation, J. Nucl. Mater. 281 (2000) 106–111, doi:10.1016/S0022-3115(00)00364-0.